In Situ Transmission Electron Microscopy of Lead Dendrites and Lead Ions in Aqueous Solution

Edward R. White,[†,‡] Scott B. Singer,[†,‡] Veronica Augustyn,[‡,§] William A. Hubbard,[†,‡] Matthew Mecklenburg,[†,‡] Bruce Dunn,[‡,§] and Brian C. Regan[†,‡,*]

[†]Department of Physics and Astronomy, University of California, Los Angeles, California 90095, United States, [‡]California NanoSystems Institute, University of California, Los Angeles, California 90095, United States, and [§]Department of Materials Science and Engineering, University of California, Los Angeles, California 90095, United States

The physical structures produced by electrochemical deposition and removal play a critical role in determining the power density, lifetime, and ultimate utility of many energy storage devices. For instance, under repeated cycling through various states of charge and discharge metal electrodes in batteries reconfigure, gradually losing performance. Dendrites in particular contribute to important failure modes for many battery technologies, including those based on lead-acid, zinc-air, lithium, and lithium-ion chemistries.[1,2] An improved understanding of the physical and chemical processes underlying dendrite formation thus is directly linked to modern challenges in power distribution and management. Dendrite growth also relates to fundamental open problems in natural, nonequilibrium pattern formation.[3,4]

Experimental investigations of dendrite formation generally incorporate at least one imaging technique. Optical imaging is the most convenient and straightforward and has a history dating back to Kepler's direct visual observations of snowflakes.[4] Current optical techniques incorporate CCD detectors and microscope objectives and allow *in situ* measurements in real time. When combined with interferometric methods, optical microscopy can also provide a determination of the local ionic (*e.g.*, Cu^{2+}) concentration.[5,6] However, as dendritic growth and morphology are known to depend on atomic-scale surface kinetics,[7] efforts to employ higher resolution imaging techniques in the study of this problem are ongoing.

Within an electrochemical context scanning electron microscopy (SEM) or transmission electron microscopy (TEM) has historically been available only as an *ex situ*

ABSTRACT
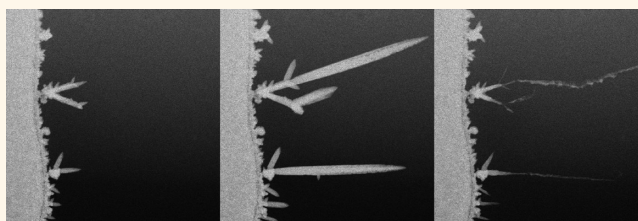
An ideal technique for observing nanoscale assembly would provide atomic-resolution images of both the products and the reactants in real time. Using a transmission electron microscope we image *in situ* the electrochemical deposition of lead from an aqueous solution of lead(II) nitrate. Both the lead deposits and the local Pb^{2+} concentration can be visualized. Depending on the rate of potential change and the potential history, lead deposits on the cathode in a structurally compact layer or in dendrites. In both cases the deposits can be removed and the process repeated. Asperities that persist through many plating and stripping cycles consistently nucleate larger dendrites. Quantitative digital image analysis reveals excellent correlation between changes in the Pb^{2+} concentration, the rate of lead deposition, and the current passed by the electrochemical cell. Real-time electron microscopy of dendritic growth dynamics and the associated local ionic concentrations can provide new insight into the functional electrochemistry of batteries and related energy storage technologies.

KEYWORDS: scanning transmission electron microscopy · STEM · *in situ* TEM · electron microscopy in liquid · dendrites · ions · water

diagnostic, because the typical electrolyte's vapor pressure is incompatible with the high-vacuum environment required in a standard electron microscope. To circumvent this problem, a low-vapor-pressure electrolyte can be used in some cases. *In situ* observations of Li-ion battery electrodes have been performed in environmental SEMs using solid polymer or low-vapor-pressure liquid electrolytes.[8,9] Very recently lithium fiber growth has been observed in *in situ* TEM experiments on nanoscale lithium-ion batteries.[10,11] These measurements were performed with an open

architecture through the use of a low-vapor-pressure ionic liquid as the electrolyte. The electrolytes chosen for these experiments hold promise for future applications, but are not yet in use commercially.

The most common electrolyte solutions are based on solvents with high vapor pressures, such as water, and thus require special measures for *in situ* TEM studies. The development of vacuum-tight, electron-transparent environmental cells for TEM has made high-resolution, *in situ* electrochemical experiments possible.[12−15] Recent achievements include the observation of galvanostatic growth of copper clusters[13] and dendrites[16] from acidified copper sulfate solution and the atomic-resolution imaging of lead sulfide nanoparticles grown *in situ*.[17] In the latter case the liquid cell included no externally controlled electrodes; the nanoparticles were produced *via* the electron-beam-induced decomposition of a multicomponent surfactant solution of lead acetate and thioacetamide.[17]

Here we report *in situ* TEM observations of the growth of crystalline lead structures on gold electrodes that are immersed in an aqueous solution of lead(II) nitrate. We observe the shorting of electrodes *via* dendrite formation, and the reproducible growth and dissolution of dendrites at particular nucleation sites. We achieve spatial resolution limited by the 2 nm pixel size programmed for the scanning TEM (STEM) beam. Quantitative image analysis of the captured movies, when compared with the current−voltage data acquired simultaneously, shows a direct relation between the total charge passed through the circuit and the amount of lead deposited. This image analysis also proves capable of revealing the variation of the Pb^{2+} ionic concentration as a function of position and time as a nearby electrode is plated with or stripped of lead.

RESULTS AND DISCUSSION

Lead's large atomic number ($Z = 82$) makes it ideal for generating dark-field STEM contrast, since the cross section for scattering electrons to large angles increases rapidly with Z.[18] Lead(II) nitrate is very soluble in water at room temperature, dissolving according to

$$Pb(NO_3)_2(s) \rightarrow Pb^{2+}(aq) + 2NO_3{}^-(aq) \qquad (1)$$
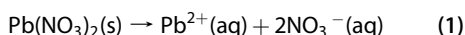
We work with a saturated (1.5 M) solution with excess, undissolved lead nitrate. Applying sufficient voltage across two electrodes in the solution leads to plating on the cathode,

$$Pb^{2+} + 2e^- \rightarrow Pb(s) \qquad (2)$$
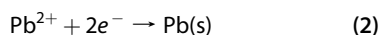
This reaction is reversible, so an electrode can serve as a source or a sink for Pb^{2+} ions. Regardless of whether the plating occurs in dendrites or in a compact layer, the products of eq 2 are crystalline with lead's characteristic face-centered cubic structure and atomic number density $n_{Pb} \simeq 33$ atoms/nm^3. Unsurprisingly,

these products generate excellent contrast and are easily imaged.

The reactant Pb^{2+} ions of eq 2 also generate good contrast when present at number densities comparable to those of the saturated solution. Under this condition, in the absence of any applied electrical potential gradient, there are $\simeq 0.9$ Pb^{2+} ions/nm^3 and the number ratio of H_2O molecules to Pb^{2+} ions is ~ 34 to 1. During Pb deposition the ionic concentration of Pb^{2+} ions near the electrode decreases as the ions plate out of solution, and the STEM signal decreases. As will be shown below, while an electrode is stripping (*i.e.*, when eq 2 is reversed and the Pb^{2+} ions are the products), the Pb^{2+} concentration nearby increases, leading to an increased STEM signal. Thus both Pb^{2+} concentration increases and decreases, whether induced by electrochemical reactions or applied electric potential gradients, can be visualized directly.

Before discussing the imaging of Pb^{2+} concentrations, however, we first describe the deposition product morphologies and growth behaviors observed on micrometer length scales. Figure 1 presents *in situ* STEM images illustrating how a compound dendritic structure can grow to short two electrodes in an electrochemical cell (see Supporting Information, Movie SM1). In this experiment the potential difference *V* applied between the working and counter electrodes is being ramped at 17 mV/s in a triangular waveform between ±1.3 V, as in cyclic voltammetry (see Supporting Information for voltammogram). In the first frame (a), the working electrode is visible, it is at a potential $V = +1.24$ relative to the counter electrode, and the time derivative d*V*/d*t* is negative. In the frames that follow, a tree-like dendritic formation enters the field of view from the direction of the counter electrode and grows until it makes contact with the working electrode, shorting the cell. Coincident with the short-circuit the potential difference *V* changes from 1.17 to 0.4 V, a value determined by the programmed current limit of 1 μA. The time from the first appearance of the dendritic forest until the short is established is 4.8 s, during which the dendrite's maximum growth rate is ~ 2 μm/s.

From the time series it is clear that the dendrites grow from the tip and not the base. Two different growth morphologies are evident in this structure: a denser, flower-like morphology more common near the counter electrode, and a blade-like morphology such as the one that makes the final point contact with the working electrode. The formation is quasi-two-dimensional: in at least one place a blade appears to grow over or under a flower, but the main branches are longer than 10 μm, a length much greater than the fluid layer's thickness. In all cases branches with blade-like morphology appear at right angles to each other. This observation is evidence of the critical role played by crystal surface energy anisotropies in determining the growth direction,[19] as will be discussed later.
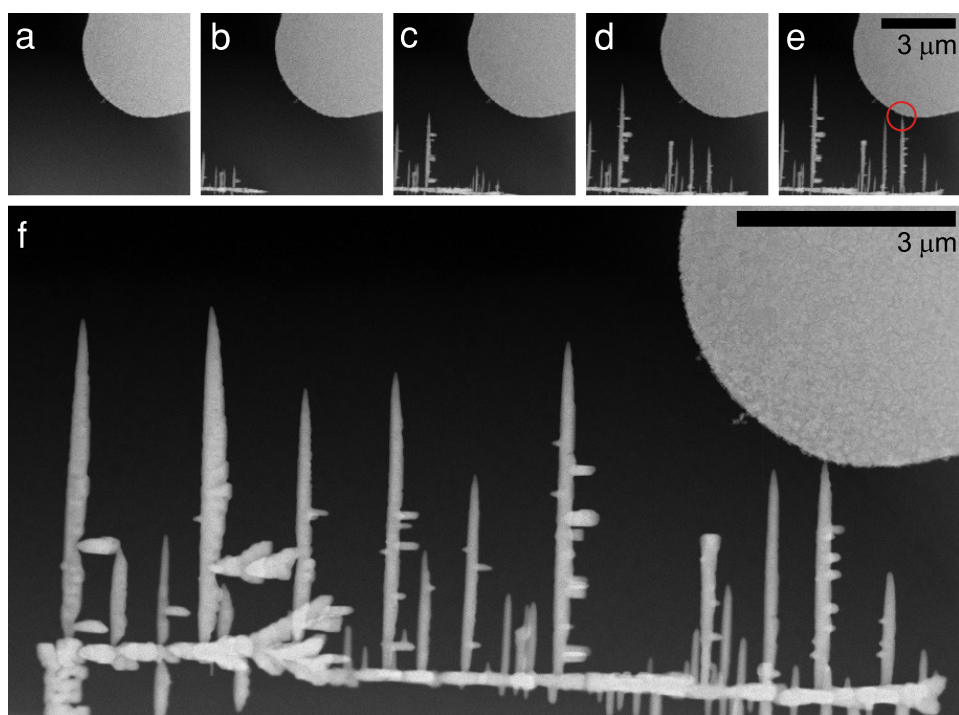
Figure 1. Time series of STEM images showing a dendritic forest that grows to short-circuit two electrodes (see also Supplementary Movie SM1). Images a−e are successive frames acquired 1.14 s apart, while the final image (f) was acquired 10 min after frame e. The working electrode, which consists of polycrystalline gold, appears in the upper right-hand corner of each frame. A similar counter electrode is outside the field of view in the direction of the opposing corner. The electrodes are shorted when contact is made at the point circled in frame e.

Finally, branches extending off of the vertical segments are generally directed toward the working electrode and not away, indicating that the bias in the growth direction is local as well as global. This bias may be attributed to the electric potential and concentration gradients between the two electrodes.

Removing the dendritic structure proves to be difficult, which highlights the tenacity of the problems presented by dendrite formation. Figure 2 shows how the dendritic forest of Figure 1 alternately grows, shrinks, and then grows again as V is stepped from −0.3 to 0.3 V and then to 1.0 V. See also Supporting Information, Movie SM2. Initially (frame a) the short of Figure 1 has been broken near the counter electrode with a 1 mA current. The remaining dendritic structure is thus at a cathodic potential and is plating lead. When the potential is reversed, the current surges and the structure begins stripping, which eventually causes the connection to the working electrode to be broken (frame b). Bringing V to an even more positive value initiates dendritic growth that begins at the counter electrode, reconnects to the remaining, previously isolated structure (frame c), and then re-establishes the short (frame d). The prevalence of right angles seen in the initial structure of Figure 1 is not evident in the structure's regrowth (Figure 2d), indicating that the second round of plating alters the previously regular geometric constraints on nucleation sites for new branches. Eventually the dendritic structure is almost

completely removed with a voltage sequence customized in accordance with real-time feedback provided by the *in situ* imaging.

The STEM signal is sensitive to the time variation of the ionic concentration. As captured by digital analysis of the indicated region of interest (ROI) in Figure 2, the stripping process is associated with a marked increase in the STEM signal R acquired from the regions neighboring the dendritic structure. This increase, which is readily apparent in the halo that appears in Figure 2b, starts to decay when the dendritic structure loses its connection to the working electrode (see also Movie SM2). A second current pulse and an associated dip in the signal from the ROI are coincident with the resumption of plating on the dendritic structure. The correlation between the gross morphological changes to the dendritic structure and the ROI signal indicates that the STEM beam experiences additional scattering from the Pb^{2+} ions in solution. The background concentration of these high-Z ions rises during stripping as ions are driven into solution and drops during plating as ions deposit out of solution (or when the effective size of the stripping electrode changes due to a disconnection event). The impressive size of the contrast changes (more than 20%) produced here suggests that other, lower-Z solutes can also be visualized with this technique.

Dendrites can be grown and shrunk controllably and repeatedly with step-like changes between potentials
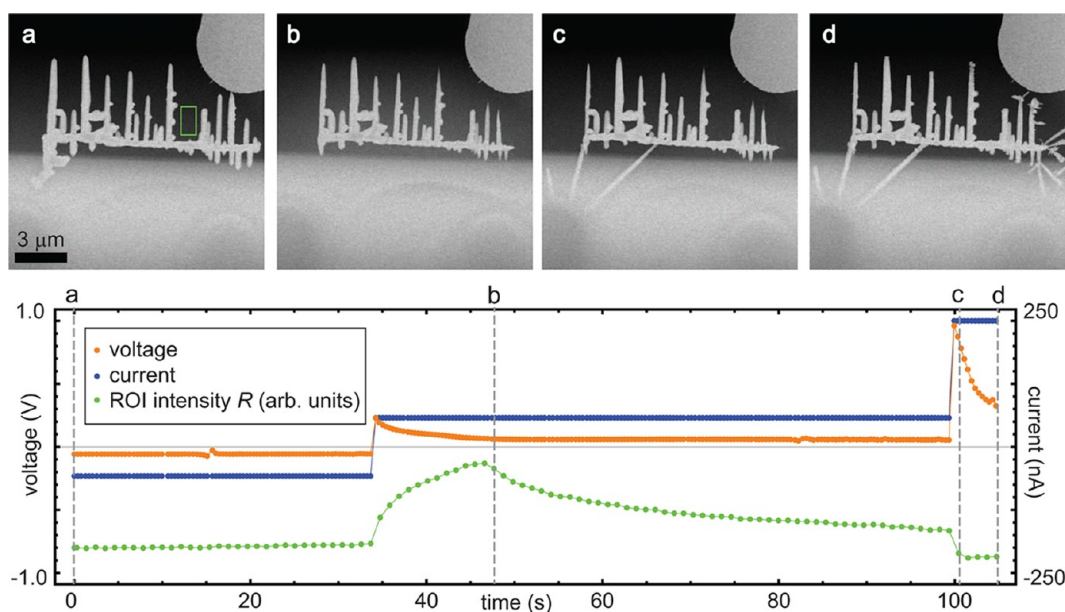
Figure 2. Time evolution (frames a–d) of the dendritic structure of Figure 1 and the corresponding applied electrical potential and measured electrical current (see also Supplementary Movie SM2). The increased brightness in the lower half of frames a–d is caused by the additional thickness of the membrane window near its edge. The intensity R from the ROI indicated by the green box in the first frame grows while the structure is stripping and decays thereafter, which demonstrates the STEM beam's sensitivity to the Pb^{2+} concentration.

with alternating polarities. Figure 3 shows images from two consecutive full cycles (out of a sequence of 43; see Supporting Information, Movie SM3, for a partial sequence) of lead dendrite growth and collapse on a gold electrode. A thin (~100 nm) layer, shown to be polycrystalline lead *via* dark-field TEM imaging, is evident in all of the images and is not present on a pristine electrode. Small dendritic structures coat this layer almost uniformly during the growth phase, but the largest dendrites repeatedly grow from special, protruding sites that do not completely disappear, even at the end of the stripping phase (frames a, g, and l). Dendritic growth is again seen to occur mostly at the tips. During the stripping phase the longest dendrites collapse first, but material loss is more uniformly distributed along a dendrite's length. This lack of time symmetry leads to the wispy structures seen in, for example, frames f and k, and in some cases causes a dendrite remnant to become detached from the electrode that initiated its formation. At their thinnest these wisps are ≲10 nm across.

As has been seen previously with *ex situ* SEM measurements,[20] the size and aspect ratio of the dendrites can be altered by adjusting the cycling waveform. We observe longer, narrower dendrites appearing when the cycling frequency is low. Alternatively, if the stripping is interrupted and left incomplete, the subsequent plating phase shows a wider array of dendritic branch growth directions, with blades nucleating throughout the structures that remain from the previous cycle.

The voltage steps responsible for the reproducible dendrite growth have associated current pulses that decay over some tens of seconds, as shown in Figure 3. The secondary cathodic current peaks that occur ~20 s after the voltage switches from 0.3 to −1.3 V are not correlated with any visible event and thus may correspond to chemistry outside the field of view (FOV). The same plot also shows an ROI intensity R indicative of the background Pb^{2+} concentration, and the global scattered STEM intensity G over the entire FOV. The latter statistic provides a measure of the total amount of lead deposition in the FOV; it rises while the dendrites are growing and falls as they collapse. Comparing the ROI intensity to the global intensity, it is clear that within a single frame of the potential change the plating process has scavenged most of the available Pb^{2+} ions in the FOV, leaving the ROI at a decreased, constant level set by the rate of mass transport toward the electrode. The promptness of the collapse of the local Pb^{2+} concentration upon the initiation of plating is also reflected in a small dip in G that occurs before the dendrites start to grow; evidently the prompt loss of signal from Pb^{2+} ions is not entirely compensated by the gain from plated Pb, when averaged over the entire FOV. During stripping the ROI intensity steadily increases until the dendrites are gone, at which point it levels off or decreases slightly as the ions diffuse away.

To determine the chemical composition of the electrodeposits, we have performed *ex situ* cyclic voltammetry control experiments and *in situ* select-area electron diffraction (SAED). The cyclic voltammetry experiments confirm the reversibility of the Pb plating and that PbO is not formed directly at the potentials reached in the *in situ* TEM experiments (see Supporting Information).
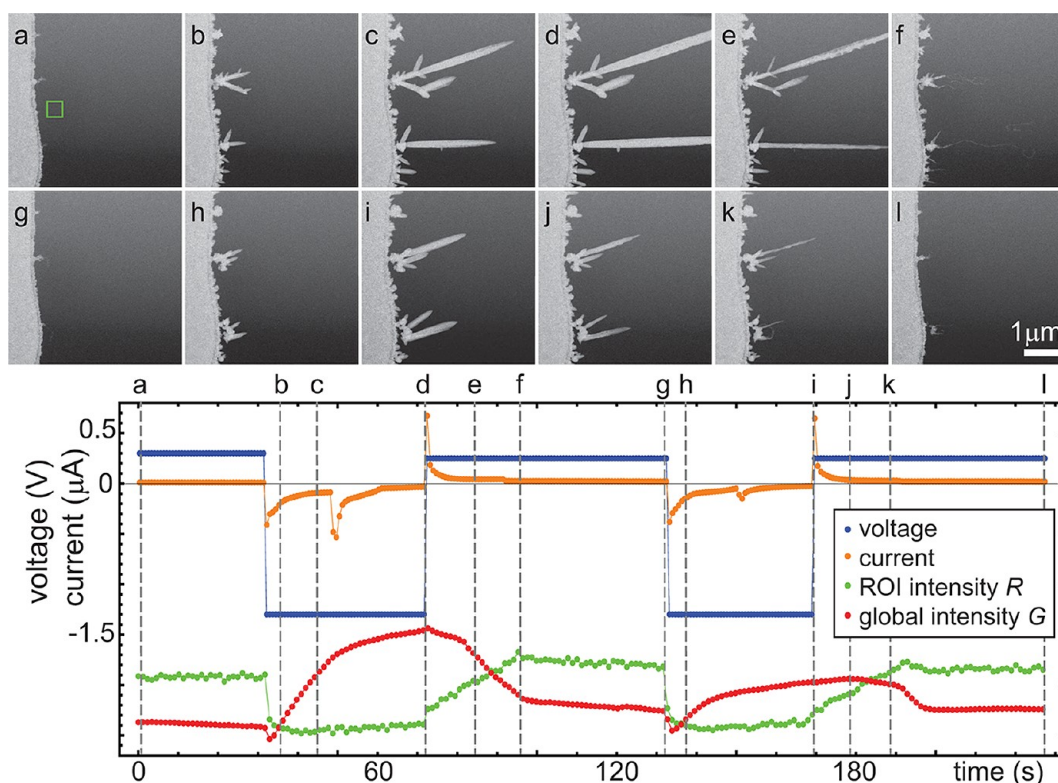
Figure 3. Repeated dendrite growth and collapse (see also Supplementary Movie SM3). The rows of frames a—f and g—l are taken from consecutive cycles, with the individual frame times indicated on the current—voltage plot below. Certain nucleation sites consistently nucleate larger dendrites. Also shown on the current—voltage plot are the STEM intensity R from the ROI indicated by the green box in frame a, and the global intensity G over the entire field of view as a function of time. Both have been rescaled and offset for display purposes.
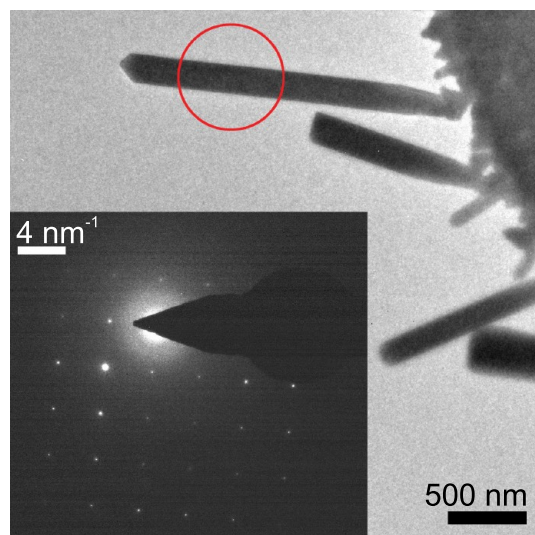

Figure 4. TEM image and associated *in situ* SAED of a blade-like dendrite immersed in the growth solution. The diffraction pattern (inset) acquired from the selected region (red circle) shows that the dendrite is lead, a single crystal, and oriented with its growth axis in the [100] direction.

The absence of PbO deposits is consistent with previous studies that found that oxide forms only after drying in an oxygenated environment.[21] The presence of solid Pb is confirmed with *in situ* electron diffraction. Figure 4 shows a TEM-mode micrograph of several blade-like

dendrites with uniform edges and clear faceting. SAED on one of the dendrites reveals that it is a single crystal of lead (fcc, lattice parameter $a = 4.95$ Å).

In addition to verifying their chemical composition, the SAED gives important information on the growth dynamics of the dendrites. The dendrite highlighted in Figure 4 has its primary growth direction (blade length) along the [100] crystal axis and its secondary growth direction (blade width) along the [010] crystal axis. These observations together with the observed prevalence of right angles in the large-scale morphology of compound dendritic structures (*e.g.*, the tertiary dendrite of Figure 1) indicate that crystalline anisotropy plays a dominant role in determining the preferred growth directions. Previously it has been noted that the preferred growth directions of Pb dendrites are ⟨100⟩ for high current densities and ⟨110⟩ for low current densities, with the crossover occurring near 1 A/cm^2 (ref 19). While we see examples of the 60° angles associated with ⟨110⟩ growth (*e.g.*, Figure 3c), the 90° morphology is far more common. Thus the dendrite growth is occurring closer to the high current density regime.

Combining traditional electrochemical transport measurements with simultaneous *in situ* STEM imaging shows that the two techniques return complementary information. Figure 5 presents STEM micrographs acquired as a gold electrode goes through two cycles of
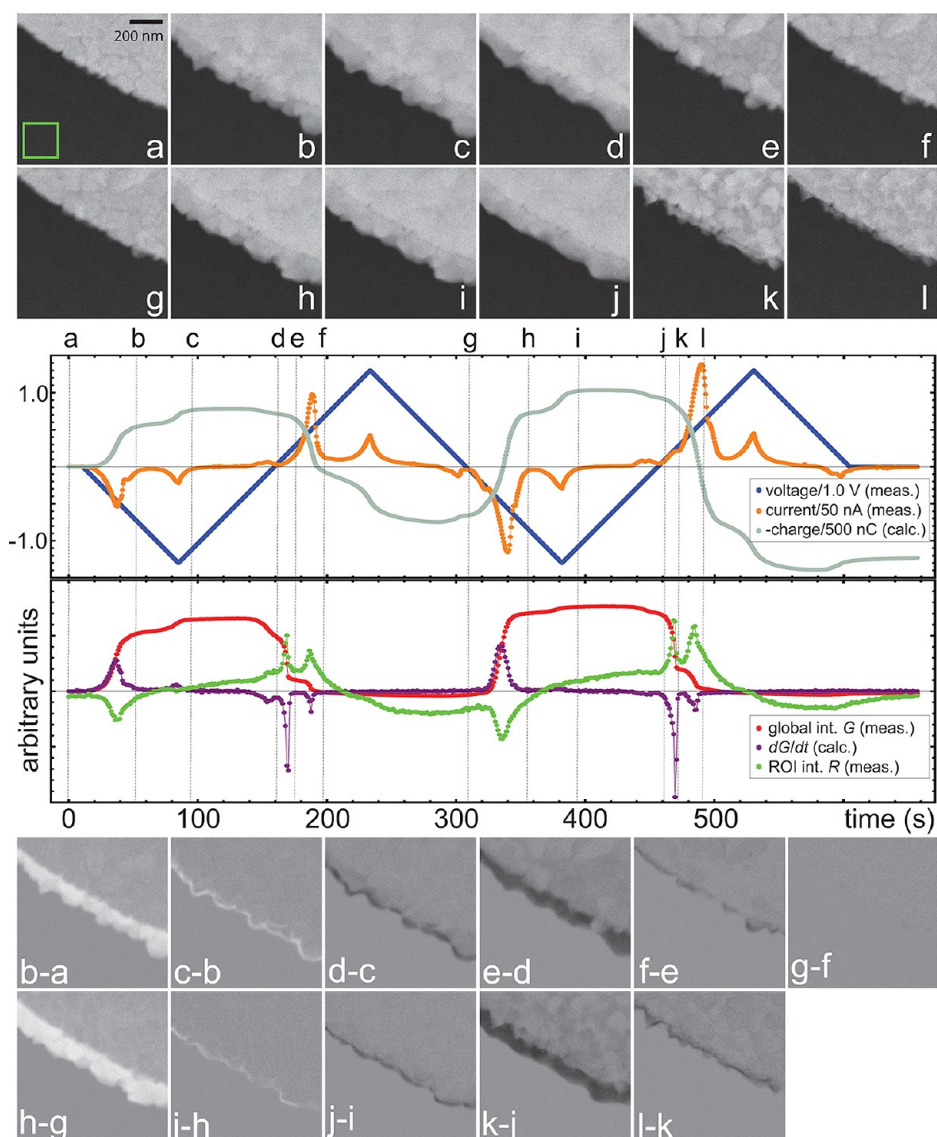
Figure 5. Triangle wave deposition at 17 mV/s (see also Supplementary Movie SM4 and other Supporting Information). (Top) Frames a–l show the growth and stripping of a ~150 nm thick lead layer on an initially pristine (frame a) polycrystalline gold electrode through two complete cycles of cyclic voltammetry. The frame times are indicated on the accompanying time evolution plot, where the electrical parameters V, I, and Q show agreeable correlations with the image parameters G, dG/dt, and R. The global intensity G parallels Q, while dG/dt and the ROI intensity R (green box in frame a) follow I modulo a sign, in some cases with higher spectroscopic resolution. (bottom) Plated layer thickness changes are highlighted in images constructed by computing the difference between the indicated frames.

Pb plating and stripping. It also shows plots that synchronize the results of a frame-by-frame digital image analysis with the electrical transport measurements. Here the potential is varying smoothly between ±1.3 V at 17 mV/s, a moderate rate that more often results in the deposition of a compact lead layer, as opposed to the dendrites that can be produced with rapid potential changes. (For more information see Figure S1 in the Supporting Information and ref 19.) The plating initiates at a potential of −0.2 V and peaks near −0.5 V, as indicated by the cathodic electrical current. A second cathodic current peak begins around −1.1 V and is still increasing in magnitude when the voltage ramp reverses direction.

The STEM images a–l and the corresponding difference images show features that can be qualitatively matched with the time evolution of the electrical current. For instance, in the first half-cycle most of the plating occurs between frame a and frame a and frame b. A second, more subtle stage of growth, representing ~20 nm of Pb, occurs between frames b and c. This additional plating is coincident with the second, smaller, cathodic current peak beginning around −1.1 V. The difference images b-a and c-b show the two distinct growth phases by highlighting the addition of new material between the displayed frames. Near the end of the first half-cycle the current becomes positive while the voltage is still negative; this

reversal is reflected in the slight thinning of the plated layer between frames c and d and highlighted in the difference image d-c. Most of the stripping from the portion of the electrode shown in Figure 5 occurs between frames d and e. Finally, after a full cycle (frame g) the electrode has returned to a near approximation of its initial condition (frame a). Because the stripping is not complete, the electrode's effective surface area is slightly larger, which may help explain the steady increase in the size of the electrical current peaks throughout the course of this data set.

Along with the voltage V and the current I, the negative of the charge $Q = \int I \, dt$ is plotted in Figure 5, where the integration has been performed numerically with a Riemann sum. Digital analysis of the STEM images returns statistics that can be directly compared with the measured I and calculated Q. As shown in the lower part of the plot of Figure 5, the global scattered STEM intensity G, which is primarily determined by the thickness of the plated layer, faithfully reproduces the main features of the curve describing the charge transferred between the electrodes during the negative potential half-cycles. During the positive half-cycles plating is occurring on the electrode outside the FOV, and thus G is insensitive to the corresponding charge transfer.

In addition to G, Figure 5 shows the time derivative dG/dt and the scattered intensity R from an ROI away from the electrode. The numerical derivative has been evaluated using a two-point difference quotient, *i.e.*, without smoothing. When the electrode is plating rapidly, dG/dt becomes large and positive while R becomes large and negative with a nearly identical time signature. This correspondence indicates that the background concentration of Pb^{2+} (reflected in R) drops as the ions plate onto the electrode (reflected in G and its time derivative). These signals also mirror the behavior of the electrical current I.

For stripping the effects are similar, with two important differences. First, the peaks change sign, as expected. Second, the single distinct peak appearing in I is split into two peaks in dG/dt and R. This split can be understood by noting that the electrical transport measurements necessarily average over the entirety of both electrodes. The peak in I is broadened by the position variation of the ionic concentrations across the electrodes, while the derivative dG/dt reflects only the local chemistry in the FOV. The ionic concentration measured directly by R, while dominated by the local chemistry, shows some broadening due to the effects of diffusion. However, in both cases the *in situ* STEM imaging clearly resolves two separate peaks where the electrical transport measurement detects only one. Because STEM imaging of the deposition products and reactants performs a prompt spatial average that is local and controlled in comparison to the blind current−voltage measurement, it may be able to

improve on the resolution of more traditional, impedance-based spectroscopic techniques.

Each peak shown in Figure 5 has not been identified with a specific chemical reaction. For instance, the small cathodic peak in I at −1.1 V is accompanied by continued Pb plating, as seen in G and in the difference images c-b and i-h. However, this second peak also implies the appearance of new reactions at this potential. Hydrogen evolution is one possibility, although the gas would have to be forming outside the FOV or going straight into solution, since bubble formation would give obvious contrast.[22]

Under certain circumstances the *in situ* STEM imaging can detect the variation in the Pb^{2+} ionic concentration with millisecond time resolution. Simple metal cations in aqueous solution at room temperature typically[23] have diffusion constants D on the order of 10^{-9} m^2/s, which implies a displacement of 30 μm within a single ~1 s frame time. However, the line-to-line scan time of the electron beam is substantially shorter (2.2 ms for 512 pixel × 512 pixel images acquired with a frame period of 1.14 s), allowing time-resolved observation of diffusion phenomena on submicrometer length scales. Figure 6 shows two instances of the time evolution of the Pb^{2+} ionic concentration, where this evolution is revealed by changing the potential on the imaged electrode shortly after the frame scan has initiated. The images a0−b0 represent the difference of two successive frames, which removes time-independent intensity variations such as those caused by a gradient in the membrane thickness. Here data captured before the potential change, shown near the top of the images a0−b0, is uniformly gray with slightly more noise in the electrode due to the larger signal there.

Once the potential reverses polarity in a0, a light region and a dark region appear at the electrode boundary, with the former indicating a layer of plated lead and the latter a concomitant drop in the Pb^{2+} concentration nearby. Moving down the frame, which corresponds to moving forward in time, we see both regions expand to the right, with the plated layer growing to ~100 nm in thickness and the Pb^{2+}-depleted region expanding out to the edge of the FOV 4 μm away. The plated layer is not completely uniform, but shows two or three locations with incipient dendrites. At the bottom of the frame the Pb^{2+}-depleted region has retracted slightly from its maximum extent, probably because the electrode begins to curve away from the FOV just past the lower boundary.

Frame b0 of Figure 6 shows the time reversal of the processes seen in frame a0: the electrode is stripping and the Pb^{2+} concentration jumps locally. This particular instance of stripping has been chosen for display because the collapsing dendrites have relatively small aspect ratios and terminate less than 900 nm away from the electrode. Thus the electrode boundary more closely approximates a spatially uniform Pb^{2+}
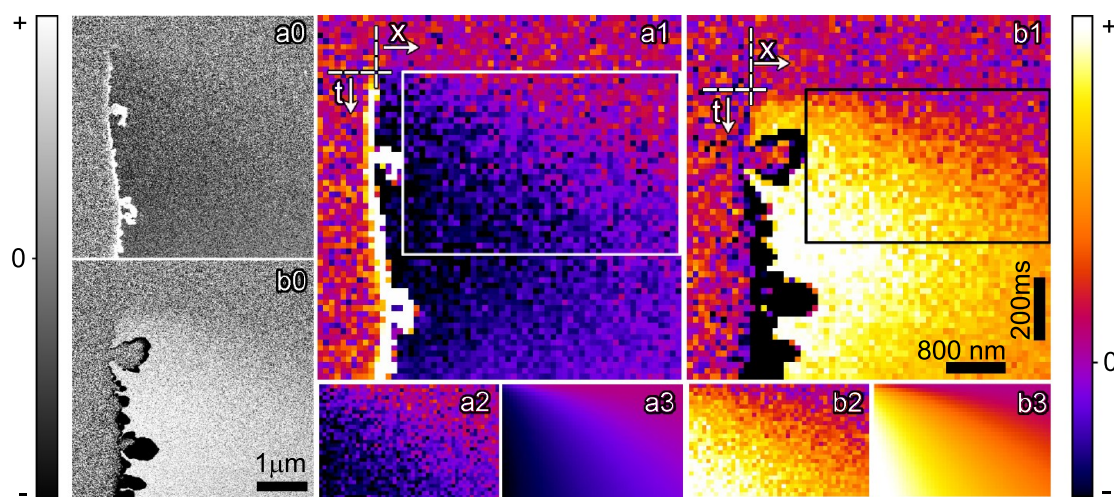
Figure 6. Time evolution of the Pb^{2+} ionic concentration. Images a0 and b0 are constructed by subtracting two consecutive 1.14 s frames in Movie SM3 (see also Figure 3), giving lighter or darker regions where the intensity increases or decreases, respectively. The STEM beam is scanning from top to bottom. During the acquisition of image a0 (b0) the potential V on the electrode shown switches polarity and begins plating (stripping) lead, which creates the white (black) regions on the electrode boundary. Images a1 and b1 depict the same events with 8×8 spatial binning and rescaling of the intensities to enhance contrast. Data (a2−b2) extracted from the boxed regions in a1−b1 are fit to eq 3 with t increasing down and x to the right. The best fits (a3−b3) return $D = 1.3$ and 1.5×10^{-11} m^2/s, respectively.

source. As in a0, once initiated, the changes spread gradually with increasing distance toward the bottom of frame b0, showing clear evidence of the time evolution of both the plated layer thickness and the ionic concentration.

To estimate the effective diffusion constant of the Pb^{2+} ions, we take our environmental cell to be strictly two-dimensional, which neglects, for instance, the plating and stripping occurring on top of the electrode (the electrode is not opaque to the STEM beam and shows intensity variation in phase with the deposition cycling). We also neglect the migration current, which may not be small compared to the diffusion current, and the spatial inhomogeneities that occur along the electrode surface. Finally, we choose regions that are more than one radius of curvature away from the electrode corner (not visible) for detailed analysis. With these approximations we can model the ionic concentration n in the selected regions of a1−b1 using the one-dimensional, time-dependent diffusion equation $\partial n/\partial t = D \, \partial^2 n/\partial x^2$, where the spatial coordinate x increases from $x = 0$ to the right and the time t increases from $t = 0$ moving downward in frames a2−b2 of Figure 6. The appropriate solution $n(x,t)$ to this diffusion equation is given by

$$\frac{n(x, t) - n_0}{n_\infty - n_0} = \text{erf}(x/2\sqrt{Dt}) \qquad (3)$$

where n_∞ is the background ionic concentration at large distances from the electrode and erf is the error function. We have enforced the boundary condition that the Pb^{2+} concentration at the electrode $n(x = 0,t)$ goes from n_∞ to n_0 at $t = 0$.

Applied to the difference data, eq 3 gives a satisfactory qualitative description (Figure 6, a3−b3) of the concentration plumes observed during plating and stripping. To perform the fit, we have assumed that changes in the STEM intensity are proportional to $n(x,t)$ and allowed for two adjustable parameters: D and a term proportional to $(n_\infty - n_0)$. We find the magnitude of the diffusion constant D to be in the range $(1-2) \times 10^{-11}$ m^2/s for both plating and stripping ($N = 56$), which helps explain how the millisecond time resolution afforded by STEM imaging is sufficient to resolve concentration variations propagating over a few hundred nanometers.

Previous investigations have found that, in the limit of infinite dilution, Pb^{2+} has a diffusion constant $D_0 = 9.4 \times 10^{-10}$ m^2/s (ref 24) and that this value decreases with increasing concentration to 2.7×10^{-10} m^2/s for 48 mM solution.[25] The theory of diffusion in concentrated electrolyte solutions such as the one used here is not entirely developed.[26] The small effective diffusion constants and correspondingly long time constants (see, for example, Figure 2) observed may reflect ion−ion interactions in the concentrated solution, structuring of the liquid near the charged electrode, hindering of free diffusion by the membrane surface, and the inadequacy of our simplifying assumptions.[27−29] Future experiments are planned to enable a more quantitative analysis.

CONCLUSION

Here we have presented *in situ* STEM observations of the electrodeposition and stripping of lead on polycrystalline gold electrodes from a 1.5 M aqueous solution of lead nitrate. Lead can be induced to deposit in a compact coating or as dendrites, with the latter morphology being more likely with abrupt potential

changes. Individual dendrites are crystalline and grow from their tips most commonly along a ⟨100⟩ crystal axis. The magnitude of the current passed through the electrochemical cell shows excellent correlation with the observed rate of Pb deposition. The discrepancies observed arise because the electrical transport measurement is sensitive to chemical reactions occurring over an area 100 times larger than the STEM FOV. Such averaging effectively reduces the spectroscopic resolution of the transport measurement in comparison to the STEM observations. Finally, STEM imaging can detect variations in the local Pb^{2+} concentration with subsecond and submicrometer temporal and spatial resolution, respectively. Because the contrast changes generated by Pb^{2+} are so large and easily detected, we expect that it will be possible to generalize this technique to visualize lighter and less soluable solutes. With its ability to provide real-time, high-resolution images of both the reactants and the products in electrochemical processes, *in situ* fluid cell STEM promises to become a powerful tool for solving dendrite formation problems in energy storage devices.

METHODS

Our fluid cell design and construction procedure has been described previously[22,30] and has elements in common with those of others.[12−17] The electrolyte solution is imaged in the TEM through two membranes fabricated from 19 nm of Si_3N_4 and 850 nm of SiO_2 grown on a 200 μm thick Si(100) wafer. A KOH etch reveals a 30 μm × 30 μm square window in a 2.1 mm × 2.1 mm silicon chip, and the membrane window is subsequently thinned by an HF vapor etch until it appears colorless when viewed in an optical microscope. An environmental chamber is constructed by epoxying together two such silicon chips back-to-back, with their electron-transparent membrane windows aligned. On one of the chips are polycrystalline gold electrodes patterned *via* optical lithography. A saturated solution of $Pb(NO_3)_2$ (99.5%, SPI-Chem) in deionized water is sealed between the two chips. Lead nitrate is chosen because its high solubility in water and large atomic number make it a good candidate solute for demonstrating the direct imaging of solvated ions. No spacer is used, but the surface corrugation from the gold electrodes ensures a chip spacing greater than 130 nm. This spacing places a lower limit on the fluid layer thickness.

The environmental cells are imaged using a biasing sample holder (Hummingbird Scientific) in an FEI Titan 80-300 TEM operated at 300 kV. Standard TEM, diffraction, and STEM modes are employed. STEM images are recorded with a Fischione model 3000 annular dark-field detector using a beam current of 57 pA, a convergence semiangle of 11 mrad, and a detector inner angle of 35 mrad. All STEM images presented are 512 pixel × 512 pixel, with the exception of Figure 1f. The resolution in each image is limited by the pixel size programmed for the STEM beam. The highest resolution data presented has a 2 nm pixel size. A Keithley 6430 Sub-Femtoamp Remote Sourcemeter is used to perform the *in situ* current−voltage measurements. The *in situ* current−voltage measurements are performed without a reference electrode. *Ex situ* cyclic voltammetry measurements use a macroscopic gold working electrode, an Ag/AgCl reference electrode, and a Pt foil or glassy carbon counter electrode. See the Supporting Information for the *ex situ* cyclic voltammogram. Digital image analysis is performed using the Labview software system (National Instruments).

REFERENCES AND NOTES

1. Arora, P.; Zhang, Z. M. Battery Separators. *Chem. Rev.* **2004**, *104*, 4419–4462.
2. Bruce, P. G.; Freunberger, S. A.; Hardwick, L. J.; Tarascon, J.-M. $Li-O_2$ and Li-S Batteries with High Energy Storage. *Nat. Mater.* **2012**, *11*, 19–29.
3. Langer, J. S. Instabilities and Pattern Formation in Crystal Growth. *Rev. Mod. Phys.* **1980**, *52*, 1–28.
4. Libbrecht, K. G. The Physics of Snow Crystals. *Rep. Prog. Phys.* **2005**, *68*, 855–895.
5. Rosso, M.; Chassaing, E.; Fleury, V.; Chazalviel, J. N. Shape Evolution of Metals Electrodeposited from Binary Electrolytes. *J. Electroanal. Chem.* **2003**, *559*, 165–173.
6. Devos, O.; Gabrielli, C.; Beitone, L.; Mace, C.; Ostermann, E.; Perrot, H. Growth of Electrolytic Copper Dendrites I: Current Transients and Optical Observation. *J. Electroanal. Chem.* **2007**, *606*, 75–84.
7. Tang, S.; Backofen, R.; Jincheng, W.; Zhou, Y.; Voigt, A.; Yu, Y.-M. Three-Dimensional Phase-Field Crystal Modeling of fcc and bcc Dendritic Crystal Growth. *J. Cryst. Growth* **2011**, *334*, 146–152.
8. Bridel, J.-S.; Azais, T.; Morcrette, M.; Tarascon, J.-M.; Larcher, D. *In Situ* Observation and Long-Term Reactivity of Si/C/CMC Composites Electrodes for Li-Ion Batteries. *J. Electrochem. Soc.* **2011**, *158*, A750–A759.
9. Dolle, M.; Sannier, L.; Beaudoin, B.; Trentin, M.; Tarascon, J.-M. Live Scanning Electron Microscope Observations of Dendritic Growth in Lithium/Polymer Cells. *Electrochem. Solid-State Lett.* **2002**, *5*, A286–A289.
10. Liu, X. H.; Zhong, L.; Zhang, L. Q.; Kushima, A.; Mao, S. X.; Li, J.; Ye, Z. Z.; Sullivan, J. P.; Huang, J. Y. Lithium Fiber Growth on the Anode in a Nanowire Lithium Ion Battery during Charging. *Appl. Phys. Lett.* **2011**, *98*, 183107.
11. Ghassemi, H.; Au, M.; Chen, N.; Heiden, P. A.; Yassar, R. S. Real-Time Observation of Lithium Fibers Growth inside a Nanoscale Lithium-Ion Battery. *Appl. Phys. Lett.* **2011**, *99*, 123113.
12. Williamson, M. J.; Tromp, R. M.; Vereecken, P. M.; Hull, R.; Ross, F. M. Dynamic Microscopy of Nanoscale Cluster Growth at the Solid-Liquid Interface. *Nat. Mater.* **2003**, *2*, 532–536.
13. Radisic, A.; Vereecken, P. M.; Hannon, J. B.; Searson, P. C.; Ross, F. M. Quantifying Electrochemical Nucleation and Growth of Nanoscale Clusters Using Real-Time Kinetic Data. *Nano Lett.* **2006**, *6*, 238–242.
14. Zheng, H. M.; Smith, R. K.; Jun, Y. W.; Kisielowski, C.; Dahmen, U.; Alivisatos, A. P. Observation of Single Colloidal Platinum Nanocrystal Growth Trajectories. *Science* **2009**, *324*, 1309–1312.
15. de Jonge, N.; Ross, F. M. Electron Microscopy of Specimens in Liquid. *Nat. Nanotechnol.* **2011**, *6*, 695–704.
16. Ross, F. M. Electrochemical Nucleation, Growth and Dendrite Formation in Liquid Cell TEM. *Microsc. Microanal.* **2010**, *16*, 326–327.

17. Evans, J. E.; Jungjohann, K. L.; Browning, N. D.; Arslan, I. Controlled Growth of Nanoparticles from Solution with *In Situ* Liquid Transmission Electron Microscopy. *Nano Lett.* **2011**, *11*, 2809–2813.

18. Spence, J. C. H. *High-Resolution Electron Microscopy*; Oxford University Press: Oxford, 2003.

19. Wranglen, G. Dendrites and Growth Layers in the Electrocrystallization of Metals. *Electrochim. Acta* **1960**, *2*, 130–143.

20. Popov, K.; Stojilkovic, E.; Radmilovic, V.; Pavlovic, M. Morphology of Lead Dendrites Electrodeposited by Square-Wave Pulsating Overpotential. *Powder Technol.* **1997**, *93*, 55–61.

21. Sawatani, S.; Ogawa, S.; Yoshida, T.; Minoura, H. Formation of Highly Crystallized β-PbO Thin Films by Cathodic Electrodeposition of Pb and its Rapid Oxidation in Air. *Adv. Funct. Mater.* **2005**, *15*, 297–302.

22. White, E. R.; Mecklenburg, M.; Singer, S. B.; Aloni, S.; Regan, B. C. Imaging Nanobubbles in Water with Scanning Transmission Electron Microscopy. *Appl. Phys. Express* **2011**, *4*, 055201.

23. Koneshan, S.; Rasaiah, J. C.; Lynden-Bell, R. M.; Lee, S. H. Solvent Structure, Dynamics, and Ion Mobility in Aqueous Solutions at 25°C. *J. Phys. Chem. B* **1998**, *102*, 4193–4204.

24. Sato, H.; Yui, M.; Yoshikawa, H. Ionic Diffusion Coefficient of Cs^+, Pb^{2+}, Sm^{3+}, Ni^{2+}, SeO_4^{2-} and TcO_4^- in Free Water Determined from Conductivity Measurements. *J. Nucl. Sci. Technol.* **1996**, *33*, 950–955.

25. Wong, S. M.; Abrantes, L. M. Lead Electrodeposition from Very Alkaline Media. *Electrochim. Acta* **2005**, *51*, 619–626.

26. Dufreche, J.-F.; Bernard, O.; Durand-Vidal, S.; Turq, P. Analytical Theories of Transport in Concentrated Electrolyte Solutions from the MSA. *J. Phys. Chem. B* **2005**, *109*, 9873–9884.

27. Morris, R. B.; Franta, D. J.; White, H. S. Electrochemistry at Pt Band Electrodes of Width Approaching Molecular Dimensions— Breakdown of Transport-Equations at Very Small Electrodes. *J. Phys. Chem.* **1987**, *91*, 3559–3564.

28. Bockris, J. O.; Reddy, A. K. N.; Gamboa-Aldeco, M. E. *Modern Electrochemistry*; Plenum Press: New York, 1998.

29. Bullard, J. W. Approximate Rate Constants for Nonideal Diffusion and their Application in a Stochastic Model. *J. Phys. Chem. A* **2007**, *111*, 2084–2092.

30. White, E. R.; Mecklenburg, M.; Shevitski, B.; Singer, S. B.; Regan, B. C. Charged Nanoparticle Dynamics in Water Induced by Scanning Transmission Electron Microscopy. *Langmuir* **2012**, *28*, 3695–3698.